Chinese Society of Aeronautics and Astronautics
& Beihang University

Chinese Journal of Aeronautics

FULL LENGTH ARTICLE

Seamless morphing trailing edge flaps for UAS-S45 using high-fidelity aerodynamic optimization

Mir Hossein NEGAHBAN, Musavir BASHIR, Victor TRAISNEL, Ruxandra Mihaela BOTEZ *

LARCASE Laboratory of Applied Research in Active Controls, Avionics and Aeroservoelasticity, École de Technologie Supérieure, Université du Québec, Montreal H3C1K3, Canada

Abstract The seamless trailing edge morphing flap is investigated using a high-fidelity steady-state aerodynamic shape optimization to determine its optimum configuration for different flight conditions, including climb, cruise, and gliding descent. A comparative study is also conducted between a wing equipped with morphing flap and a wing with conventional hinged flap. The optimization is performed by specifying a certain objective function and the flight performance goal for each flight condition. Increasing the climb rate, extending the flight range and endurance in cruise, and decreasing the descend rate, are the flight performance goals covered in this study. Various optimum configurations were found for the morphing wing by determining the optimum morphing flap deflection for each flight condition, based on its objective function, each of which performed better than that of the baseline wing. It was shown that by using optimum configuration for the morphing wing in climb condition, the required power could be reduced by up to 3.8% and climb rate increases by 6.13%. The comparative study also revealed that the morphing wing enhances aerodynamic efficiency by up to 17.8% and extends the laminar flow. Finally, the optimum configuration for the gliding descent brought about a 43% reduction in the descent rate.

1. Introduction

The aeronautics industry has a significant impact on greenhouse gas emissions, as thousands of airplanes, ranging from personal aircraft to commercial and military jets, fly every day. This huge number of daily flights contributes to the emission of a large amount of CO_2 into the atmosphere. This situation was demonstrated during the COVID-19 pandemic, as satellite images show the CO_2 emissions before and during the pandemic; there was a considerable decrease in the CO_2 emissions.[1] According to the Carbon Global Project,[2] the drop

* Corresponding author.
E-mail address: ruxandra.botez@etsmtl.ca (R.M. BOTEZ).

in flights dramatically reduced the Carbon emissions during the worldwide lockdown compared to the other sources, including surface transport and industry. Their findings indicate that during the peak of world-wide lockdown (March, April, and May 2020), the 75% reduction in air traffic accounted for 60% of the carbon emission reduction, while the surface transport accounted only for a 36% reduction (being the second after aviation), which is nearly half. Carbon emission reduction is therefore one the highest-priority goals in the aeronautics industry due to its undeniable impact on the climate.

Following the main goal of green aviation, numerous projects both in industry and in academia, most of which are collaborative industrial-academics projects, have focused on reducing CO_2 emissions. Among these, at the flight trajectory level, Airbus' UpNext [3] is one of the most recent projects. Their proposed "Fello'fly" concept offers a reduction of carbon emissions by at least 5% per trip according to operational evaluations. However, most of the studies in green aviation are at the level of aircraft design. These include aerodynamic, propulsive, and structural aspects of aircraft, all of which are inter-connected. For example, in aerodynamics, many studies have been conducted on drag reduction, which leads to a reduction in fuel and power consumption.

In aerodynamics, morphing wing technology has shown a great potential to apply to next-generation environmentally friendly aircraft, due to its success in improving aircraft performance by reducing drag and fuel consumption, as well as in reducing aircraft weight. [4,5] While most of these studies are still at the conceptual level due to structural limits, ongoing research in aerodynamics and at a structural level have shown a promising future for this technology. Many morphing approaches have been examined over the past few decades from sweep,[6] twist, [7,8] winglet, [9,10] and span morphing, [11] to camber, [12–15] chord, [16] leading edge, [17–19] and upper surface [20–29] morphing. However, among these approaches, the trailing edge morphing [30] has received considerable attention due to its substantial influence in improving flight performance and reducing fuel consumption. Beyond aerodynamic analysis, structural analysis [31] as well as aerostructural analysis [32] for the trailing edge morphing approach is developing more rapidly than other morphing approaches, due to the high number of studies in this area. Different types of morphing mechanisms have been proposed, [33–40] some of which have been prototyped and successfully wind-tunnel tested. [41–45]

Numerous morphing mechanisms have been proposed at the conceptual design level for different morphing configurations, such as morphing leading edge, morphing trailing edge, [46,47] or morphing upper surface. However, few successful tests have been reported at the flight test level. Among these, AFTI/F-111 mission adaptive wing, [48] is the pioneering project, a joint project of UASF, NASA and Boeing, in which a successful flight test was performed by F-111 fighter aircraft equipped with active camber morphing. Unfortunately, due to actuation system complexity and weight penalties, the project was closed. The Adaptive Complaint Trailing Edge (ACTE) project, among the U.S Air Force Research Laboratory (AFRL), NASA and Flexsys [49–51] is another flight test level project. In the ACTE project, a Gulfstream III business jet equipped with morphing trailing edge wings was tested at the altitude of 40000 ft(1 ft = 0.304 8 m), and it was the only practical test of morphing wings in recent years. This work showed that this

technology was dependable after over 50 hours of flight tests, and it documented its ability to improve aerodynamic performance.

The potential benefits of trailing edge morphing in terms of improving aerodynamic performance and thereby reducing fuel consumption have been illustrated in recent studies. Abdessemed et al. [52] compared morphing trailing edge flaps to conventional hinged flaps, both in steady and unsteady conditions to investigate the aerodynamic performance of real-time morphing. They showed that the baseline wing with a hinged flap and zero deflection caused an increase in drag and a reduction in lift due to the spanwise and chordwise gaps. The comparison of the morphing versus hinged flap showed that morphing trailing edge increased the lift by up to 40% at similar drag coefficients and improved the overall aerodynamic efficiency by 45%. In Ref.53, the same authors evaluated this morphing configuration in a 2D transient study through dynamic meshing, and also analyzed the unsteady behavior of morphing flaps. [54] They showed that 22% higher lift was generated and a 25% drag reduction was achieved for the morphing trailing edge flap, which led to a 40% improvement in aerodynamic efficiency for pre-stall angles of attack. In addition, the stall angle was increased by 2° compared to that of the hinged flap. Several studies have been conducted on NASA's Variable Camber Continuous Trailing Edge morphing Flap (VCCTEF) system. In Refs. 55, 56, Ting et al. conducted aerodynamic and structural optimizations that found a gain of 2%–16% in lift-to-drag ratio and up to a 8.4% in drag reduction for a range of flight conditions.

In a joint project between NASA and Boeing, Urnes and Nguyen [57] investigated the VCCTEF system for future transport aircraft, that improved aircraft performance in terms of lift and drag, while reducing aircraft weight and increasing its maneuverability, including rolling performance. Their work showed that a VCCTEF system could accomplish two performance objectives: (A) efficient high lift capability for take-off and landing, and (B) cruise drag reduction through the control of the flexible wing twist shape. A multidisciplinary optimization was also conducted on a VCCTEF system by Lebofsky et al. [58], through which the drag reduction was obtained by reducing the wing stiffness.

Woods et al. [59] introduced a compliant morphing flap transition section (sealing the gaps between wing main body and flap) by addressing the side-edge gaps in the spanwise direction. They showed that in the absence of transition, a strong vortex emerged near the gaps; however, with a transition section, the downstream roll-up vortex disappeared. CFD simulation results also showed that by using complaint transition section, lift was increased, drag was reduced and a 7% increase in lift-to-drag ratio was obtained. To reduce lift-induced drag, Ninian and Dakka [60] simulated and compared the trailing edge morphing flap with a conventional wing flap. Their comparison of a non-optimized morphing wing with a conventional wing showed an increase in lift of up to 10.8% and a lift-to-drag ratio improvement of up to 13.6% for the optimized morphing wing. They also performed an experimental acoustic analysis and showed that using a morphing wing decreased the noise level up to 50% in comparison to using a conventional wing. The effects of deploying spanwise morphing trailing edges on wings were also studied in Refs. 61–63.

Lyu and Martins [64] used the gradient-based optimization to perform a multipoint optimization for an adaptive trailing

edge wing. Drag reductions of 1% in a morphing trailing edge wing at off-design conditions and of 5% at on-design conditions were obtained. They computed the cruise fuel consumption for different fight phases and found that by using the morphing trailing edge, nearly 1% fuel consumption reduction could be obtained.

A new morphing trailing edge design concept was introduced by Communier et al. [65], in which the deformation was performed by use of small vertical incisions. The comparison of aerodynamic coefficients revealed that this morphing design achieved a lower drag coefficient than that of a conventional design. They also showed that the morphing trailing edge had a higher lift-to-drag ratio and outperformed a hinged flap for angles of attack ranging from −10° to 10°.

Bashir et al. [66] investigated the shape optimization of an UAS-S45 airfoil by evaluating the morphing at the trailing edge at the leading edge. For the morphing leading edge, the lift coefficient was increased by 21% and the stall angle was delayed by 3°. For the trailing edge morphing, by considering drag minimization as an objective function, they found a 26% gain in lift coefficient and an 8% gain in maximum lift coefficient, compared to the baseline airfoil. They also showed that trailing edge morphing improved the endurance by approximately 10.25% compared to that of the unmorphed airfoil. Dumont [33] proposed a trailing edge morphing mechanism that applied two flexible surfaces on the wings' lower and upper surfaces. This morphing approach was applied to both the flaps (inner wing) and the ailerons (outer wing). By performing a gradient-based optimization, Dumont obtained a 2.6% gain in the objective function as well as a 0.595° reduction in angle of attack.

To eliminate the gaps between flaps and the main wing configuration, Khorrami et al. [67] patented an elastic morphing structure for the side edges of the trailing edge flap. This structure significantly reduced the aeroacoustic noises associated with the discontinuities of side edge gaps without compromising an aircraft's cruise efficiency. This innovative configuration was capable of elongation in a chordwise direction, bending and twisting as needed, and when not deployed, it conforms to the chordwise cross-section of the flap's side edge. In an experimental study, Rivero et al. [68] evaluated the FishBack morphing configuration with a hinged flap and the baseline airfoil; they found a lower drag penalty for the morphing configuration with a similar lift coefficient that led to a greater lift to drag ratio, that gave from 50% to 200% improvement over the baseline airfoil.

The above-mentioned studies are just some of the recent noteworthy studies on the morphing trailing edge. In this study, the aim is to achieve a high-fidelity optimization of the Seamless Morphing Trailing Edge (SMTE) flap for most of the flight conditions (climb, cruise, descent) of the whole flight envelope. To the authors knowledge, no optimization has been conducted on a morphing seamless flap to maximize the flight performance made possible by this morphing configuration. This present study is conducted on an UAS-S45, an unmanned aerial system that was designed and manufactured by Hydra Technologies, a Mexican company. This UAS-S45 is mainly designed for surveillance and reconnaissance missions. Multiple morphing studies have been conducted on this UAS-S45 at our Research Laboratory in Active Controls, Avionics and Aeroservoelasticity (LARCASE), as shown in

Fig. 1, and its aerodynamic model has been extensively studied. [69]

In this paper, the seamless morphing flap was optimized using a high-fidelity gradient-based methodology that uses the discrete adjoint method on the three main flight phases of the whole flight envelope, including climb, cruise, and descent, with the specified objective functions for each flight condition. For the climb condition, the aim was to find the optimum deflection of the SMTE flap to maximize the climb rate, for the cruise flight, the main purposes were the range and endurance maximization, and for the descent flight, the main objective was to reduce the descent rate by the morphing of the SMTE flap.

2. Methodology

Eliminating the gap between the wing and its edge flaps gave many advantages in terms of reducing the flow turbulence around the junctions by extending the laminar flow, reducing drag and noise, and thus, generating more lift force. Therefore, sealing the gaps in trailing edge flaps, which are considered the main control surfaces on a wing, and generating a smooth flap deformation will unquestionably improve the wings' aerodynamic performance. In this study, the SMTE flap is studied for the whole flight envelope for the UAS-S45 by finding the optimum deformation for each flight condition. Fig. 2 illustrates the SMTE flap. As indicated, the SMTE flap covers 30% of the chord length and 41% of the wings' semi-span by including the transition sections.

Given that the main goal of this study is the aerodynamic optimization of the SMTE flap, a high-fidelity optimization is conducted to obtain the optimum morphing configuration for SMTE flaps in different flight conditions, including climb, cruise, and descent. This optimization is performed separately for each flight condition with its specified objective function. Gradient-based optimization coupled with the discrete adjoint method in conjunction with the high-fidelity flow solver Open-FOAM. This process generates the UAS-S45 wing design using the Free-Form Deformation (FFD) parametrization method. The following sections describe the overall framework used in this paper.

2.1. Gradient-based optimization- IPOPT optimizer

The optimization problems solved by using the gradient-based method are generally expressed in the following form:

$$\min_{x \in R_n} f(x) \tag{1}$$

where the optimum value of $f(x)$ is found by calculating the partial derivatives or gradients of design variables, which leads the search directions to the optimum possible values of $f(x)$. Some algorithms, such as gradient descent, which is the basic algorithm of the gradient method, only requires the first derivatives of the function of interest (Jacobian matrix), whereas other algorithms also require the second derivatives (Hessian matrix). While there are many gradient-based algorithms, the most suitable algorithm is determined according to the optimization problem, including whether it is linear or nonlinear, constrained, or unconstrained, etc. In this study, the optimization problem is a nonlinear constrained problem
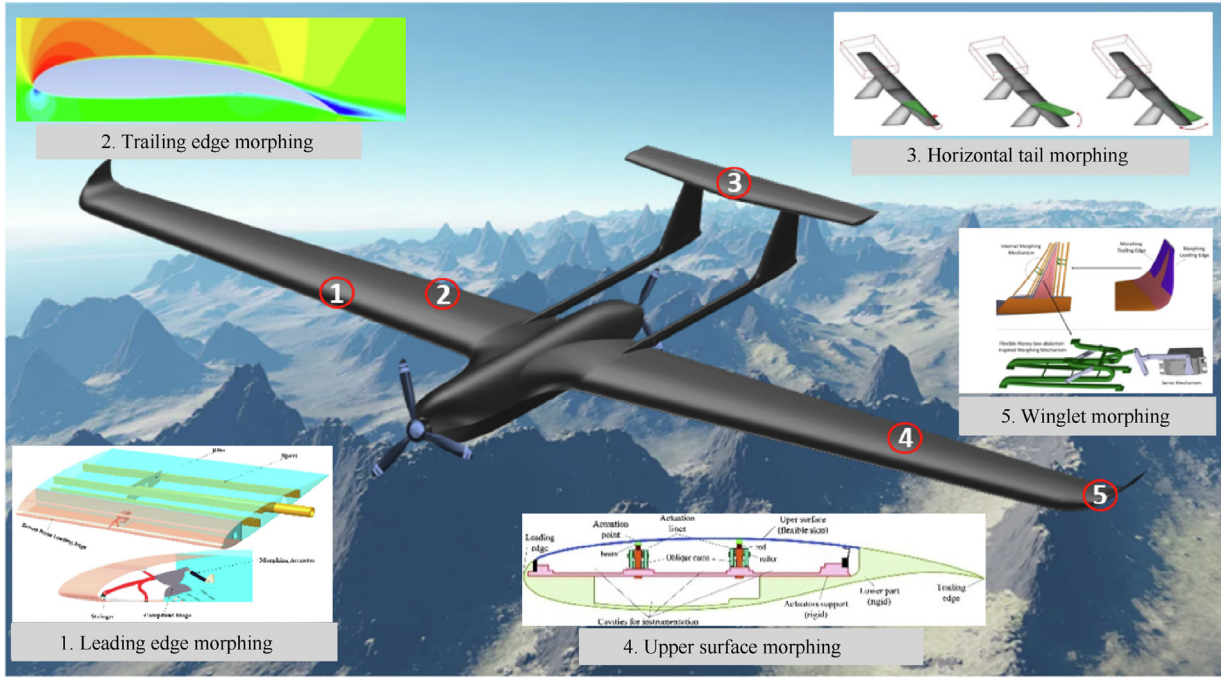
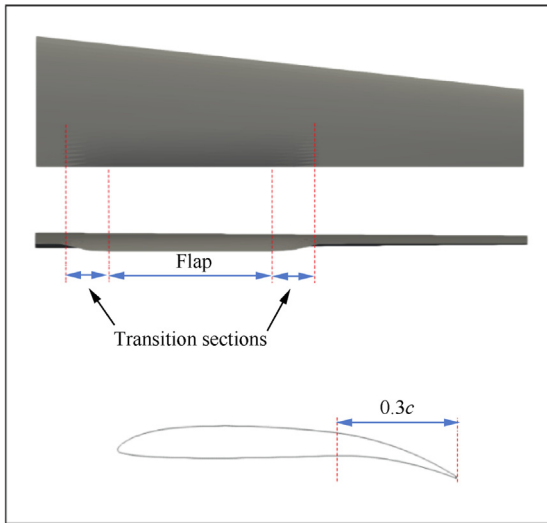**Fig. 1** Morphing studies on UAS-S45 conducted at LARCASE.

Fig. 2 Schematics of a SMTE flap.

that contains equality and inequality constraints. The algorithm established in this study is the Interior Point Optimizer (IPOPT), first developed by Wächter and Biegler in 2006 [70] and applied to solve nonlinear and continuous constraint problems. In this method, the line searches are based on filter methods. The IPOPT optimizer employs the Automatic Differentiation (AD) technique to find the first and second derivatives of the objective function (Jacobians and Hessians, respectively); however, quasi-Newton methods, such as the Broyden-Fletcher-Goldfarb-Shanno algorithm (BFGS) are used, when the second derivatives are not available. The general form of problems solved by the IPOPT method is [71]

$$\begin{cases} \min f(x) \\ \text{subjected to}: \ LB \leq g(x) \leq UB \\ \qquad\qquad lb \ \leq x \leq \ ub \end{cases} \tag{2}$$

where x are the design variables, $f(x)$ the objective function, $g(x)$ the constraint function, and LB and UB denote the lower and upper bounds for the constraint function, respectively. Likewise, lb and ub represent the lower and upper bounds for the design variables, respectively.

2.2. DAFoam optimization framework

The optimization methodology performed in this study takes advantage of a high-fidelity framework, known as the object-oriented discrete adjoint with OpenFOAM, in which the high-fidelity flow solver OpenFOAM is used in the optimization loop. This process produces results that are more accurate than those obtained by low-fidelity solvers, such as XFOIL or XFLR5, which are generally used in aerodynamic optimization. Discrete adjoint implementation in OpenFOAM was proposed by Towara and Naumann in Ref. 72, where they have used an AD for the computation of derivatives. However, the use of the AD considerably increases the computation cost for a simple problem, thus rendering the AD inappropriate for shape optimization. To extend the Discrete Adjoint (DA) implementation in OpenFOAM for solving optimization problems, the DAFoam optimization framework was developed by MDO laboratory team at Michigan University. [73] In this optimization framework, the adjoint equation's partial derivatives were computed using the accelerated Finite Difference technique (FD) rather than an AD method, this is accomplished by making discrete adjoint based optimization in OpenFOAM a feasible process, even for optimization problems with a higher number of design variables. In this optimization frame-

work, a high-level interface was established to compute the discrete adjoint derivatives by the solvers in OpenFOAM. For different solvers in OpenFOAM, the DA implementation differs in the: (A) residual and state variable vectors; (B) Jacobian matrix; and (C) method for the calculation of residuals.[73] Three child classes (sub-class) were therefore created to specify the above three variations, as well as another child class for specifying the turbulence state variables in OpenFOAM. [73] This interface thus allows the adjoint derivative to be computed using any steady-state flow solver in OpenFOAM.

In this optimization framework, a high-level interface was established between the OpenFOAM layer and Python libraries, where the former consists of the flow solver "simpleFoam", the adjoint and the graph coloring solvers, while the latter consists of three libraries for mesh deformation and optimization setup: "pyGeo" for the parametrization of surface geometry and geometric constraints computations, "pyWrap" for the deformation of volume mesh and "pyOptSparse" for the optimization (See Refs.[73], [74] for details). Fig. 3 illustrates the overall optimization process, where the OpenFOAM and Python layers are specified with different colors.

2.3. Discrete Adjoint (DA) method

The Discrete Adjoint (DA) method uses discretized Navier-stokes equations to obtain the adjoint terms by differentiating the discretized equations. In optimization problems with high number of design variables, the computation of partial derivatives of the design variables is a very expensive and demanding task. The DA method is a reversed method, which can circumvent this demanding task and therefore, can highly reduce the computation time and cost by placing the dependency of partial derivatives on the state variables, rather than on the design variables. In other words, the most time-consuming part of gradient calculations, which are dependent on design variables, is replaced by adjoint equation calculations, which are dependent upon the state variables. The number of state variables is noticeably lower than the number of design variables, thereby a huge amount of computation time is saved.

Consider $f = f(x, \omega)$ as an objective function, where x and ω are the design and state variables, respectively. The computation of the total derivatives of f is expressed as follows:

$$\frac{\mathrm{d}f}{\mathrm{d}x} = \frac{\partial f}{\partial x} + \frac{\partial f}{\partial \omega} \cdot \frac{\partial \omega}{\partial x} \qquad (3)$$

where $\frac{\partial \omega}{\partial x}$ is the only term that depends upon the number of design variables; however, this dependency can be avoided by assuming that the residuals of governing equations must be satisfied, that is $R(x, \omega) = 0$, and therefore the derivatives of residuals with respect to x are also equal to zero.

$$\frac{\mathrm{d}R}{\mathrm{d}x} = \frac{\partial R}{\partial x} + \frac{\partial R}{\partial \omega} \cdot \frac{\partial \omega}{\partial x} = 0$$
$$\text{or} \qquad\qquad (4)$$
$$\frac{\partial \omega}{\partial x} = -\frac{\partial R}{\partial x}\left(\frac{\partial R}{\partial \omega}\right)^{-1}$$

By combining Eqs. (3) and (4) through the mutual term $\frac{\mathrm{d}\omega}{\mathrm{d}x}$, one obtains:

$$\frac{\mathrm{d}f}{\mathrm{d}x} = \frac{\partial f}{\partial x} - \frac{\partial f}{\partial \omega}\left(\frac{\partial R}{\partial \omega}\right)^{-1}\frac{\partial R}{\partial x} \qquad (5)$$

In Eq. (5), the term $\frac{\partial f}{\partial \omega}\left(\frac{\partial R}{\partial \omega}\right)^{-1}$ is considered as the adjoint vector ψ, computed by solving a linear equation, called the adjoint equation (Eq. (6)).

$$\left[\frac{\partial R}{\partial \omega}\right]^{\mathrm{T}} \psi = \left[\frac{\partial f}{\partial \omega}\right]^{\mathrm{T}} \qquad (6)$$

In Eq. (6), Finite Difference method (FD) is used for the computation of the partial derivatives; however, to accelerate the computation time, the graph coloring method [75] is used, in which the Jacobian matrix is divided into subgroups in specified colors so that at least one of the elements in adjacent rows is zero, and thus elements in multiple columns located in the same group are perturbed at the same time. The objective and residual computation is done only once (see Ref. 74 for details) in this graph coloring approach, in contrast to the regular FD method, which the number of iterations for the computation of the objective and residuals reaches to millions (approximately more than 10 million for 3D problems). After the computation of partial derivatives, the PETSc library
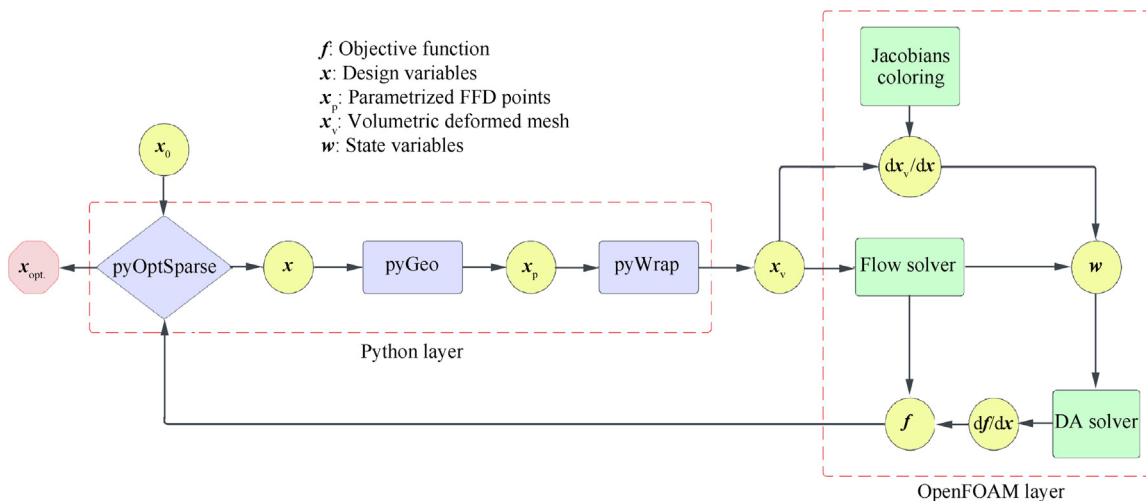

Fig. 3 Overall optimization framework.

(toolkit for advanced optimization in Python) is used to solve the adjoint equation to find the adjoint vector ψ. Finally, the last step is the computation of $\frac{\partial f}{\partial x}$ and $\frac{\partial R}{\partial x}$ in Eq. (5), which are obtained by using the Brute-Force FD approach. Ultimately, the total derivative of f can be obtained by replacing the partial derivatives of the objective function $\left(\frac{\partial f}{\partial x}\right)$ and the residuals $\left(\frac{\partial R}{\partial x}\right)$ as well as of the adjoint vector ψ in Eq. (6), as follows:

$$\frac{\mathrm{d}f}{\mathrm{d}x} = \frac{\partial f}{\partial x} - \psi^{\mathrm{T}} \frac{\partial R}{\partial x} \qquad (7)$$

The DA procedure considerably reduces the number of iterations and thus, the computation time, making the optimization problems with high number of design variables (wing or full aircraft) feasible.

2.4. Free-Form Deformation (FFD)

Wing model is generated before the optimization process and the technique used for parametrization has a substantial impact on the final optimization results. Covering a large design space with a small number of design variables could lead to an effective parametrization.[76] The FFD technique is part of the Soft Object Animation (SOA) algorithms,[77] which are considered among deformative parametrization techniques. The FFD parametrization was developed by Sederberg and Parry[77] in 1986, since then, several modifications have been added to this algorithm, that are applied to real engineering problems,[78–80] in particular to aerodynamic shape optimization.[81] In the earliest model, the control points on FFD block were defined through tri-variate Bernstein polynomials;[77] however, subsequent models have introduced tri-variate Bezier, and NURBS polynomials.[78–80] In the FFD parametrization, the studied body (aircraft or its components, such as wing) is embedded inside the FFD block, and any modification in the control points of this block deforms the inner body shape. For 3D wing or aircraft optimization problems, in which the design variables are of the order of 10^2, constructive parametrization techniques, such as NURBS, Bezier-PARSEC, and CST, which are commonly used in 2D optimization problems, are not feasible due to the high number of design variables. However, since the FFD method considers the geometry variations rather than the geometry itself,[82] the number of design variables becomes almost irrelevant, thus making it the best technique for optimization problems with numerous design variables. For instance, let $\bar{g}$ be the baseline geometry and $\Delta \bar{G}$ the geometric change or variation, so that:

$$\bar{G}_{\mathrm{defomed}} = \bar{g} + \Delta \bar{G} \qquad (8)$$

During the aerodynamic optimization, the geometric change $\Delta \bar{G}$ includes all types of variations, including twist, camber, thickness, shear, and planform deformation, as indicated below:

$$\Delta \bar{G} = \delta \bar{G}_{\mathrm{twist}} + \delta \bar{G}_{\mathrm{camber}} + \delta \bar{G}_{\mathrm{thickness}} + \delta \bar{G}_{\mathrm{shear}}$$
$$+ \delta \bar{G}_{\mathrm{planform}} \qquad (9)$$

Depending on the morphing approach, these variations are controlled by defining the degree of freedom to the FFD control points. For instance, in trailing edge morphing, the only required variation is the camber ($\delta \bar{G}_{\mathrm{camber}} > \mathbf{0}$); therefore, all other variations are confined to zero deformation ($\delta \bar{G}_{\mathrm{twist}} = \delta \bar{G}_{\mathrm{thickness}} = \delta \bar{G}_{\mathrm{shear}} = \delta \bar{G}_{\mathrm{planform}} = \mathbf{0}$).

In this paper, the FFD block is represented through the tri-variate B-spline volume, which is defined below:

$$\vec{V}(u, v, w) = \sum_{i=0}^{N_u-1} \sum_{i=0}^{N_v-1} \sum_{i=0}^{N_w-1} N_{i,m_u}(u) N_{j,m_v}(v) N_{k,m_w}(w) Q_{i,j,k} \qquad (10)$$

where N_{i,m_u}, N_{j,m_v}, and N_{k,m_w} are the basic functions, m_u, m_v, and m_w are the degrees of freedom and $Q_{i,j,k}$ is the initial block. To map the parameter space (the FFD control points) to the physical space (the embedded geometry), the Newton search method [83] is applied to the initial embedded object given by $\vec{P}(u, v, w)$.

$$\vec{P}(u, v, w) = \sum_{i=0}^{N_u-1} \sum_{i=0}^{N_v-1} \sum_{i=0}^{N_w-1} N_{i,m_u}(u) N_{j,m_v}(v) N_{k,m_w}(w) Q_{i,j,k} \qquad (11)$$

Using Eq. (12), the basic functions are calculated in all directions:

$$N_{i,l_u} = \begin{cases} 0, u_i \leq u \leq u_{i+1} \\ 1, \text{otherwise} \end{cases}$$
$$\text{and} \qquad (12)$$
$$N_{i,m_u}(u) = \frac{u-u_i}{u_{i+m_{u-1}}-u_i} N_{i,m_{u-1}}(u) + \frac{u_{i+mu}-u}{u_{i+mu-u_{i+1}}-u_i} N_{i+1,m_{u-1}}(u)$$

By obtaining the new coordinates of the embedded body (wing), the new B-splines volume is calculated and is replaced by the initial volume given in Eq. (11).

$$\vec{P}^{\mathrm{new}}(u_0, v_0, w_0) = \sum_{i=0}^{n_u} N_{i,m_u}(u_0), N_{j,m_v}(v_0), N_{k,m_w}(w_0) Q_{i,j,k}^{\mathrm{new}} \qquad (13)$$

In Eq. (13), $Q_{i,j,k}^{\mathrm{new}}$ are the coordinates of the control points after deformation, through which the new coordinates of the embedded object are obtained, given by $\vec{P}^{\mathrm{new}}$. The sensitivity of the points inside the FFD block can be obtained as follows:[84]

$$\frac{\partial P}{\partial x} = \frac{\partial Q}{\partial x} \cdot \frac{\partial P}{\partial Q} \qquad (14)$$

where x is the design variable, $P = \vec{P}(u, v, w)$ are the coordinates of the embedded body, $Q = \vec{Q}(u, v, w)$ are the coordinates of the FFD control points and $\frac{\partial P}{\partial Q}$ is the shape function. Two important factors should be noted before the optimization process. Firstly, the topology of the FFD block should be defined. The FFD block should be body-fitted, meaning that it should not be too large or far from the design surface, as the gradients received by the optimizer should be on the same order of magnitude during the optimization. Secondly, the number of control points is case-dependent, and it should be chosen depending on the studied case. In our previous work,[85] we showed how control points impacts the final optimization results and computation time. Therefore, this aspect should be considered before starting the optimization process. In this study, two types of FFD blocks are created, one corresponding to the trailing edge section (red block) and the other one corresponding to the rest of the wing (blue block) (see Fig. 3). Since we are studying trailing edge morphing, the deformation of the wing is confined to upward and downward deflections of the flap along the span. The number of control points for two blocks are 30 and 6 in the spanwise and chordwise directions, respectively, which corresponds to the total number of 360 FFD control points for the whole

wing. Fig. 3 shows the UAS-S45 wing embedded in FFD block. For a wing with SMTE flap, the control points on the flap section are free to move in the upwards and downwards directions, the rest of control points are confined to zero deflection, and thus only 52 out of the 360 control points are active (Fig. 4). Fig. 5 shows the FFD block after morphing, in which the flap is morphed along with the block deformation.

2.5. Optimization methodology

2.5.1. Solver-agnostic setup

This study seeks the optimum configuration of the SMTE flap for the whole flight envelope, including climb, cruise, and descent. Therefore, each flight condition has different objective functions, that are characterized by specific goals, as summarized in Table 1.

As indicated in Table 1, each flight condition has a different objective function, and in the cruise flight, the optimization process requires two different objectives, range, and endurance. Depending on the flight mission objective, the SMTE flap will have different configurations; for instance, if the UAV's mission objective relies on its long-distance flight, then the optimum wing configuration will be set according to the range maximization (Table 1), otherwise, if longer flight time is the mission objective, then the wing morphs to its optimum shape according to the optimum endurance configuration. Each flight condition is optimized according to its flight characteristics, including the angle of attack, altitude, and speed, and finally, the constraints and objective function. Table 2 indicates the details of each flight condition and Fig. 6 illustrates the main flight envelope for the UAS-S45.

Although the objective function for each flight condition is different, the overall optimization framework is the same for all of them. The number of geometric design variables (FFD block and control points) and geometric constraints remains the same for all optimization processes; however, the objective function is unique to each flight condition. Table 3 shows the overall optimization setup.

The above optimization setup is used for each flight condition by simply changing the objective function according to Table 1. A total number of 24 optimizations are performed to find the optimum configuration of SMTE for the whole flight envelope of the UAS-S45.
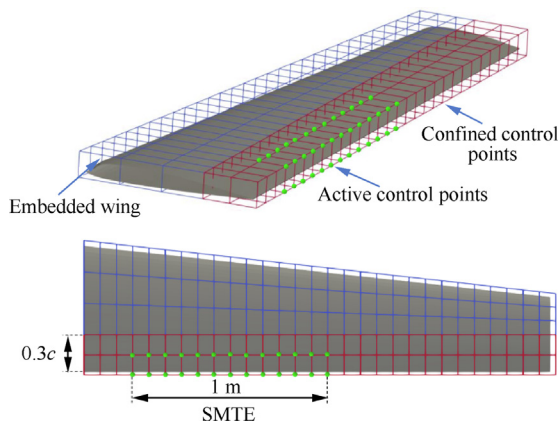

(a) Isometric

(b) Side view
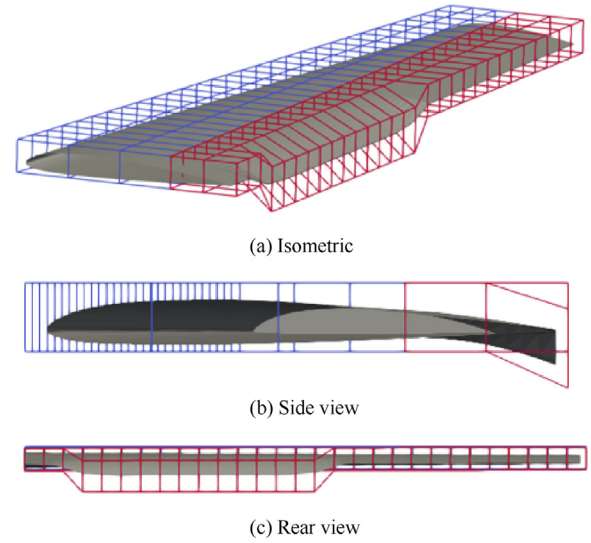

(c) Rear view

Fig. 5 FFD blocks after deformation.

Table 1 Specific goals and objective function for each flight condition.

Flight condition	Goal	Objective function
Climb	Increasing climb rate	$\min C_D/C_L^{3/2}$
Cruise	Increasing range (flight distance)	$\max C_L/C_D$
	Increasing endurance (flight time)	$\max C_L^{3/2}/C_D$
Gliding descent	Reducing descent rate	$\min C_D/C_L^{3/2}$

Table 2 Characteristics of each flight condition.

Flight condition	Speed (kt)	Altitude (ft)	Reynolds number(10^6)
Climb	65	0	1.2
Cruise - range	55	15000	0.7
Cruise - endurance	55	15000	0.7
Gliding descent	55	15000	0.7

2.5.2. Flow solver setup

As mentioned earlier, in this optimization framework, flow equations are solved using a high-fidelity solver, OpenFOAM, to extract the state variables and update the objective function in each iteration (Fig. 3). The whole flight envelope is in the subsonic regime. The incompressible Navier-Stokes equations are solved with the steady state solver "simpleFoam". The turbulence model chosen for this study is Spalart-Allmaras (S-A) model. The grid is generated in ICEM-CFD using a hexahedral structured grid (Fig. 7). Except for the boundary, to which the wing is attached and has "symmetry" boundary condition, the rest of the boundaries are defined as the "inletOutlet". In this boundary condition, when the fluid flows into and out
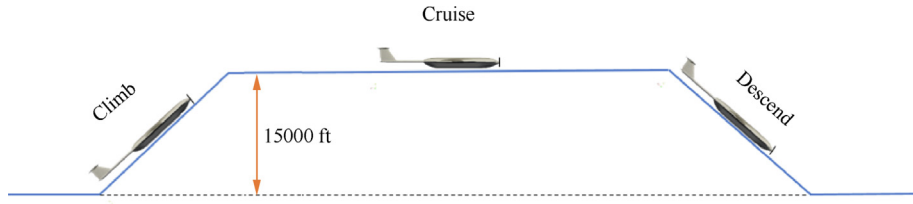

Fig. 4 FFD blocks for UAS-S45 wing.

Fig. 6 Whole flight envelope of UAS-S45.

Table 3 Overall optimization setup for each flight condition.

Function/variable	Description	Total number
Objective function		
max/min f	f: Objective function for each flight condition (Table 1)	4
w.r.t:		
Y	FFD control points	360
Subject to:		
$C_L \geq C_{Lmin}$	Constant function	1
$\alpha_{initial} = \alpha_{final}$	Constant angle of attack	1
$v \geq v_{initial}$	Volume constraint	
$-150\ \text{mm} \leq \Delta y \leq 150\ \text{mm}$	Design variable bounds	52
$\Delta y^{upper}_{z=3} = \Delta y^{upper}_{z=15}$	Linear constraint	52

of the domain, the boundary condition alternates between "fixed value" and "zero gradient", respectively.

3. Results and discussion

The results obtained from the optimization are presented in four sections, each of which represents a set of flight conditions (climb, cruise, descent) with its specified objective function. For each flight condition, the aerodynamic properties of the wing with SMTE flap are compared with those of the baseline wing. A comparison is also drawn between an SMTE flap and a hinged flap on the full UAS-S45 in the cruise flight.

3.1. Climb condition

In a climbing flight, which accounts for the first phase of the whole flight envelope, the main goal is to increase the altitude, in other words, to turn the aircraft's kinetic and internal energy into potential energy to overcome the aircraft's weight. During a straight and level flight, the required energy is provided by the engines at a specified speed; however, to increase the potential energy (altitude) at the same speed, extra power is required; the amount of this added power determines the rate at which the altitude is increased.[86] The added power is the difference between the power required for level flight and the engine's available power. Fig. 8 shows the balance of the aerodynamic forces for the UAS-S45 in climb condition.

By assuming constant speed (no acceleration), summing these forces along the climb angle (γ) gives:

$$T - D = W\sin\gamma \tag{15}$$

To obtain the power, Eq. (15) is multiplied by the velocity as follows:

$$\frac{TV - DV}{W} = V\sin\gamma \tag{16}$$

where TV and DV are the available power (P_{av}) and the required power (P_{req}), respectively. Therefore:

$$\frac{P_{av} - P_{req}}{W} = V\sin\gamma \tag{17}$$

As shown in Fig. 9, $V\sin\gamma$ is the vertical velocity of the aircraft and contributes to the rate of climb (dh/dt). As mentioned in Section 2, the main goal in climb phase is to increase the rate of climb, and, given that an aircraft's weight
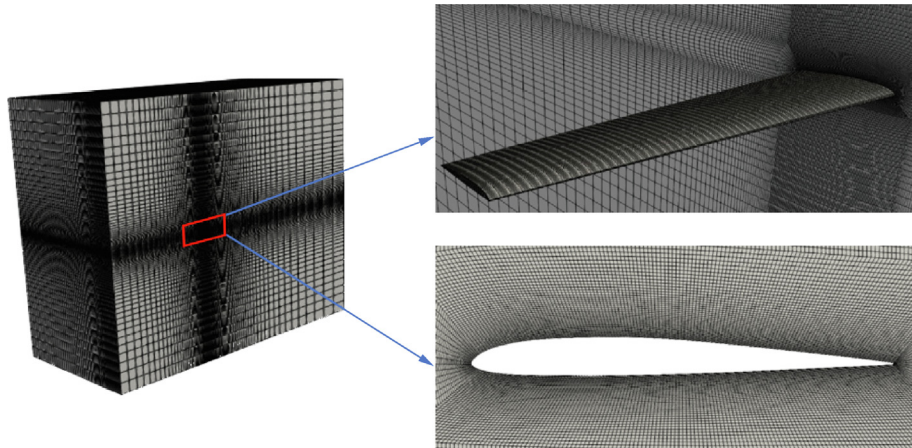

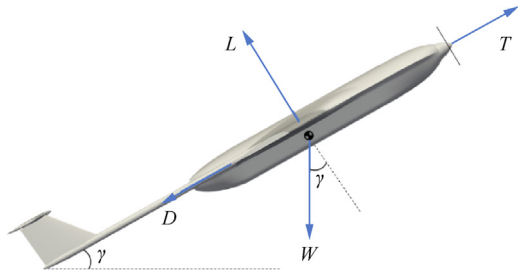**Fig. 7** Illustration of structured surface and volume mesh with hexahedral elements.

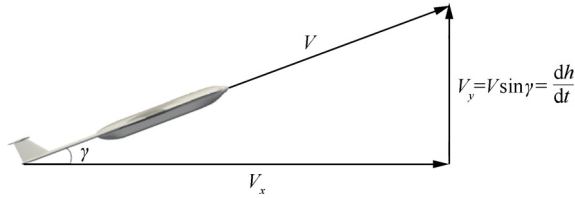**Fig. 8** Aerodynamic force balance around UAS-S45 in climbing flight condition.

Fig. 9 Illustration of rate of climb as vertical velocity.

(W) and available power (P_{av}) are constant, the only variable is the required power (P_{req}) (as given in Eq. (17)). Therefore, by reducing the required power (P_{req}), one can increase the rate of climb.

In level and straight flight, the required power is obtained from the Eq. (18): [86]

$$P_{req} = \left(\frac{2W^3}{\rho S}\right)^{1/2} \frac{C_D}{C_L^{3/2}} \tag{18}$$

where W is the aircraft weight, ρ the atmospheric density, and S the surface area. In climb, due to the climbing angle, the lift force is equal to $W\cos\gamma$; however, in this study, to use the level flight assumption ($L = W$), the small angle assumption [86] is used, where the angles below 15° are considered, or where $\cos\gamma \approx 1$. The minimum limit of this assumption is $\gamma = 5°$, where $\cos\gamma = 0.9962$, and its maximum limit is $\gamma = 15°$, where $\cos\gamma = 0.9659$, for which the maximum error is within 5%. In this study, the optimization of climb condition is performed for $\gamma = 5°$, at which the level flight assumption has the least error, 0.38%.

In Eq. (18), to reduce the required power, one can simply minimize the $\frac{C_D}{C_L^{3/2}}$ term, through which the required power is minimized (Eq. (18)) and the climb rate is increased (Eq. (17)). Therefore, the objective function to solve this optimization problem is defined as the minimization of $\frac{C_D}{C_L^{3/2}}$, leading to the goal in the climb condition, i.e., decreasing the P_{req} (Eq. (18)) and increasing the climb rate. Table 4 shows the optimization results obtained for the UAS-S45 wing in the climb condition. Note that the deflection in the downward direction is assumed positive.

It is found that the required power (P_{req}) decreases 3.8% using the downward morphing of the flap, which leads to an increase in climb rate according to Eq. (17). In this case, where the weight of the UAS-S45 is nearly 49 kg and the $P_{av} = 8$ kW, if we assume P_{req} is 5 kW, then the rate of climb becomes 61.2

m/s (Eq. (17)). However, by minimizing P_{req} by up to 3.8%, the climb rate for the UAS-S45 wing equipped with an SMTE flap becomes 65.2 m/s, equivalent to a 6.13% increase in the climb rate (Table 4).

3.2. Cruise flight

In this study, the cruise flight objective function is divided into the optimization of range and of endurance. The optimization is performed according to the mission objective. If the mission objective is to cover a long-distance flight, then the SMTE flap will have the optimum shape according to the range objective function; and if the mission objective is to increase the flight time, the optimum shape will be based on the endurance objective function, as shown in Table 1.

3.2.1. Range optimization
For a propeller-engine aircraft, the range is calculated according to Eq. (19):

$$R = -\frac{\eta_p}{\gamma_p} \cdot \frac{C_L}{C_D} \ln\left(\frac{W_1}{W_2}\right) \tag{19}$$

where η_p is the propulsive efficiency, γ_p weight-specific fuel consumption and W_1 and W_2 are initial and final aircraft weight, respectively.

According to Eq. (19), the only aerodynamic term that impacts the flight range is the lift-to-drag ratio, thus by increasing this ratio, the range will be increased. Therefore, the objective function in terms of range improvement is the maximization of the lift-to-drag ratio. Our results obtained from aerodynamic parameters, including lift, drag and lift-to-drag-ratio show the need to deploy an SMTE flap, due to its substantial improvement of aerodynamic performance over clean wing and a wing with deflected hinged flaps (Fig. 10).

As shown in Fig. 10(c), the overall aerodynamic performance of the wing with SMTE flap has increased compared to hinged flap configuration. By considering the diagrams of the lift and drag coefficients separately, it is evident that this improvement is mostly due to the excessive lift generation of the SMTE flap (Fig. 10(a)). While the drag with SMTE flap is more than that of the hinged flap at some of the angles of attack (Fig. 10(b)), this drag penalty is compensated by the excessive lift generation, which results in the overall improvement of the aerodynamic efficiency by up to 33% and 17.8% compared to clean wing and hinged flap, respectively (Fig. 10(c)). It is also shown that by increasing the angle of attack, the optimized flap deflection decreases and approaches to zero deflection, becoming similar to the performance of the baseline wing configuration. Note that the angle of deflection of the hinged flap is taken from that of the optimized SMTE flap to draw a precise comparison ($AOD_{Hinged} = AOD_{Opt. SMTE}$).

In fact, a deflecting flap during cruise flight is not efficient at every angle of attack, hence the SMTE flap performance is only efficient for a limited range of angles of attack. As shown in Fig. 10(c), after $\alpha = 2.5°$, the performance of the wing with SMTE flap degrades compared to that of the clean wing; however, for the wing with a hinged flap, the maximum best performance is only up to $\alpha = 1°$. This means that the morphing flap can perform in an extended range of α ($\alpha = 0°$ to 2.5°) compared to the hinged flap, for which better efficiency compared

Table 4 Comparison of UAS-S45 wing with and without an SMTE flap in climbing flight.

Configuration	$\gamma(°)$	Flap deflection (mm)	C_L	C_D	$\frac{C_D}{C_L^{3/2}}$	Required power (%)	Climb rate (%)
S45 + SMTE flap	5	18.4	0.75342	0.03493	0.05341	−3.8	+ 6.13
Clean wing	5	0	0.61797	0.02697	0.05552		
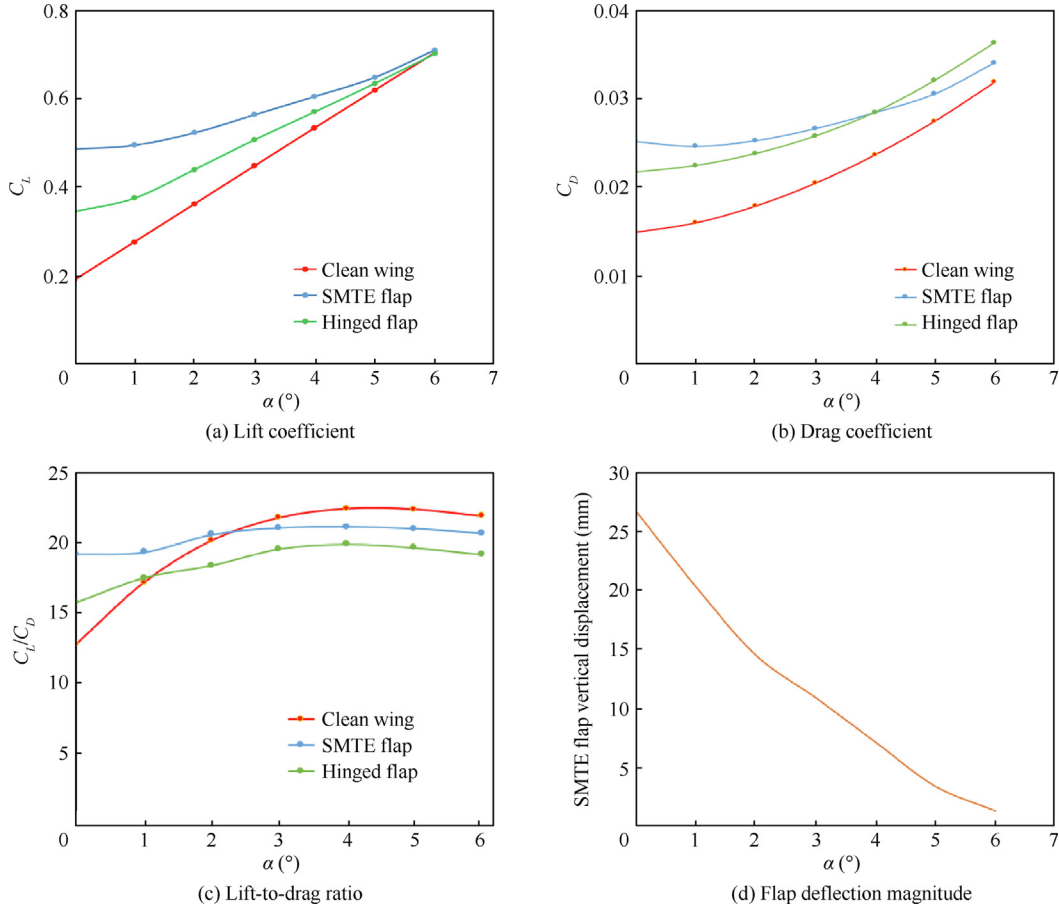
Fig. 10 Comparison of aerodynamic performance of wing with SMTE flap, hinged flap, and baseline wing configurations for various angles of attack.

to baseline wing is limited to α = 0 to 1°. Fig. 11 compares the UAS-S45 wings with deflected SMTE and hinged flaps.

In addition, Fig. 12 illustrates the whole UAS-S45 equipped with an SMTE flap on the right wing and a hinged flap on the left wing to obtain a good comparison in terms of the pressure variations, detailed in Figs. 12(a)–(c).

The pressure coefficient distribution in both chordwise and spanwise directions in Figs. 12(a)–(c) clearly show the pressure peaks around the gaps for the hinged flap, whereas for the SMTE flap, these pressure peaks have been eliminated, leading to very smooth pressure variations. These pressure peaks occur mainly because of the spillage of the flow from the pressure side to the suction side due to the presence of the gaps; for the hinged flap, this flow mixture acts as a flow control mechanism at higher angles of attack, where the flow on the pres-

sure side mixes with the separated flow on the suction side and then reattaches to the separated flow.

In addition, both the chordwise and the spanwise pressure diagrams (Figs. 12 (a)–(c)) show that for the SMTE flap, the pressure gap between the upper and lower surface of the wing is more than that of the hinged flap, which leads to the increased lift generation. This increase in pressure coefficient is due to the seamless transition section, whose contribution in the flap deformation increases the lifting surface of the wing. In contrast, for the hinged flap, these sections are solid undeformed parts of the wing, which have no contribution to the flap deflection. Elimination of the gaps in the SMTE flap extends the laminar flow on the upper surface of the wing, whereas for the hinged flap, the low-pressure contour is stopped at the start of the gap (Fig. 13(a)). The laminarity of
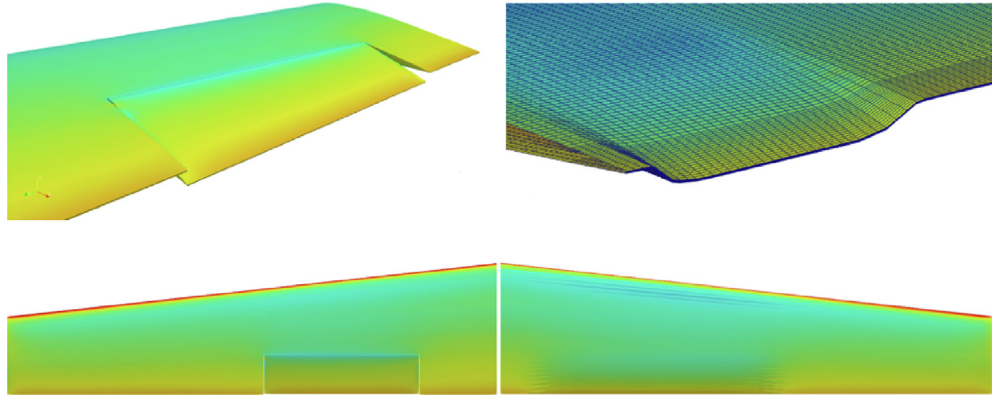
Fig. 11   Comparison of SMTE flap (right) with hinged flap (left) for cruise flight.

the flow is preserved up to the tip of the trailing edge for the SMTE flap (Fig. 13(a)). The bottom part of the pressure contours (Fig. 13(b)) also illustrates the difference in the pressure gaps between the SMTE and the hinged flap. As shown, for the SMTE flap, the maximum pressure is concentrated on the bottom surface of the whole flap due to the elimination of the gaps and the flap's smooth deformations.

The seamless characteristic of the SMTE flap enhances the flow's steadiness and diminishes its turbulent behavior due to the elimination of the gaps. As shown in Fig. 14(a), the gap in the hinged flap causes a downwash or spillage in the flow, similar to the wing tip downwash. Figs. 14(b) and (c) clearly show the difference of the flow behaviors on these flaps, as the vorticity contours indicate the recirculation of the flow between the gaps in the hinged flap, while in the SMTE flap, this recirculation disappears, and the boundary layer is more stable. The creation of the downwash (by the hinged flap) decreases the effective angle of attack of the wing, and thus the lift, wherein the seamless effect of the SMTE flap eliminates both recirculation and downwash.

Therefore, by considering the aerodynamic advantages of the SMTE flap versus the hinged flap, the efficiency of the seamless morphing flap in improving aerodynamic performance is obvious.

3.2.2. Endurance optimization

As another objective function of the cruise condition, the endurance mainly concerns the flight time, as most of the flight time is dedicated to the cruise flight condition. Depending on the engine type, the relation of the endurance to the aerodynamic properties differs. For a propeller engine, the endurance equation is defined as follows:

$$E = -\frac{\eta_p}{\gamma_p}\sqrt{2\rho S}\frac{C_L^{\frac{3}{2}}}{C_D}\left(\frac{1}{\sqrt{W_2}} - \frac{1}{\sqrt{W_1}}\right) \qquad (20)$$

where η_p is the propulsive efficiency, γ_p is the weight-specific fuel consumption, and the only aerodynamic term affecting the endurance is $C_L^{3/2}/C_D$, which is called endurance efficiency, where the lift generation is of higher priority than the drag reduction. By considering Eq. (20), the objective function for the endurance optimization of an SMTE flap is the maximization of the $C_L^{3/2}/C_D$ term. Having proven the superiority of the SMTE flap over the hinged flap in the previous section, here

the purpose is to find the optimum configuration of an SMTE flap for maximum endurance.

Figs. 15(a)–(d) show the aerodynamic properties obtained with the SMTE flap after the optimization. These properties are compared to those of a clean wing, i.e., with no flap deflection.

The optimum aerodynamic properties of an SMTE wing for maximum endurance are obtained for different angles of attack (Fig. 15). As shown in Figs. 15 (a) and (b), with flap deformation in the downwards direction, both lift and drag are increased; however, the increase in lift is more than that of the drag increase, and considering the endurance efficiency, $C_L^{3/2}/C_D$, the influence of lift is higher than that of drag; therefore, the final aerodynamic performance is improved compared to that of the clean wing. However, the endurance efficiency diagram (Fig. 15(c)) shows that the morphing configuration loses its performance as the angle of attack increases up to the $\alpha = 7°$, after which the performance of both wings becomes the same, and past this angle, the clean wing performs better than the wing with an SMTE flap. In other words, after $\alpha = 7°$, there should not be any flap deflection, since after $\alpha = 7°$, the retracted wing has its optimum endurance configuration. It should also be noted that since this is a cruise flight condition, smaller angles of attack are considered, and it is obvious that the maximum endurance occurs at the $\alpha = 0°$, where it is 61.2% higher compared to the clean wing with retracted flaps. According to UAS-S45 manual, the cruise angle is almost 2°, for which the endurance is increased by 26.78% with an SMTE flap (Fig. 15(c)).

In the same way as range, in the endurance, the deformation of the SMTE flap also approaches to zero deflection as the angle of attack increases (Fig. 15(d)). In addition, the spanwise pressure coefficient also shows a smooth variation trend near the SMTE flap, as shown in Fig. 16. At the $\alpha = 11°$, there is nearly no variation in the pressure coefficient, on both wings' upper and lower surfaces, thus indicating that the morphing wing performs like the baseline wing in terms of aerodynamic forces.

3.3. Gliding descent

The last flight condition studied in this paper is the non-powered gliding descent. In a space shuttle, non-powered or gliding descent is a normal flight condition, with no engine
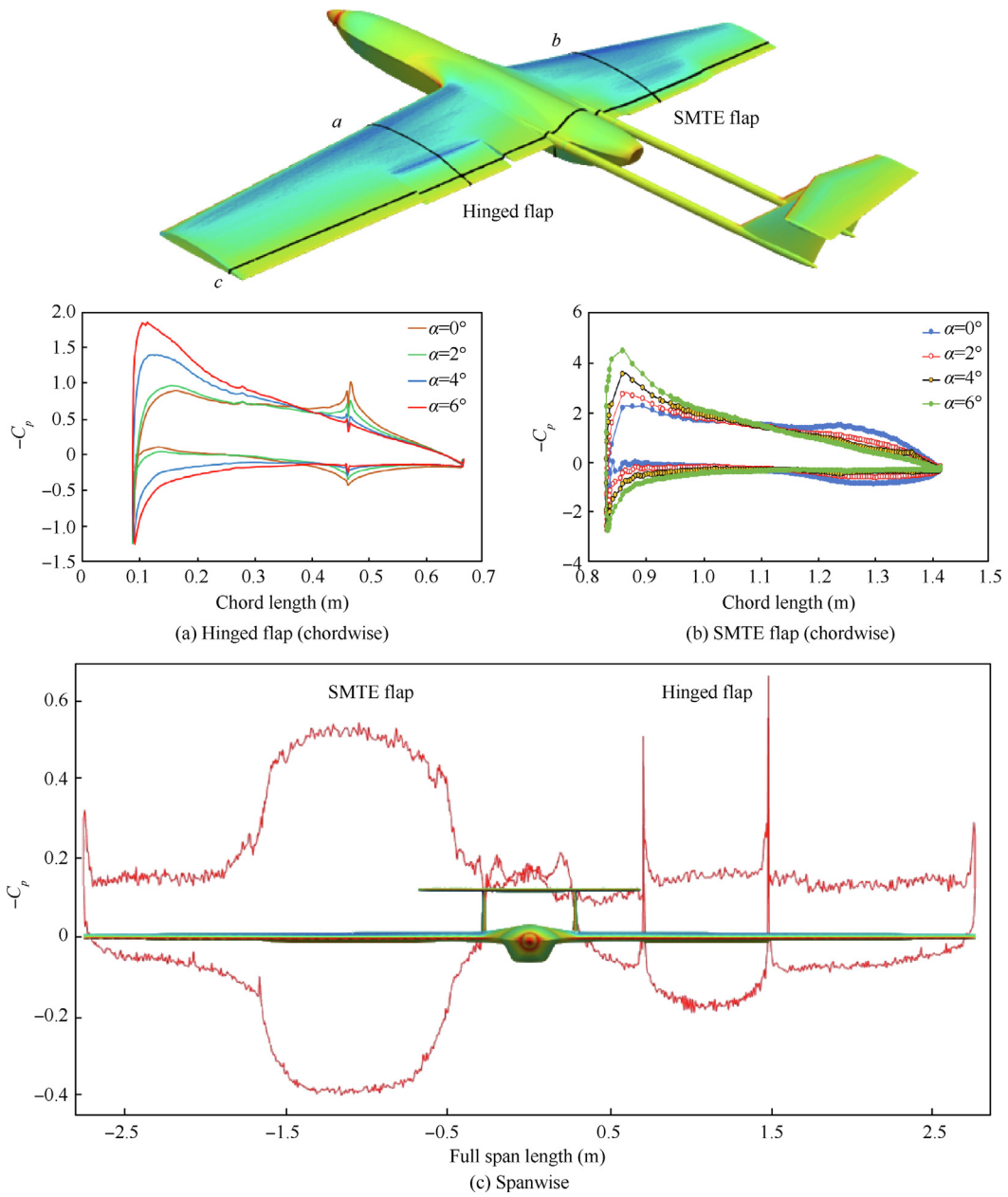
(a) Hinged flap (chordwise)

(b) SMTE flap (chordwise)

(c) Spanwise

Fig. 12 UAS-S45 equipped with an SMTE (right) and a hinged flap (left), with their pressure coefficient distribution presented in both chordwise *a* and *b*, and spanwise *c* directions.
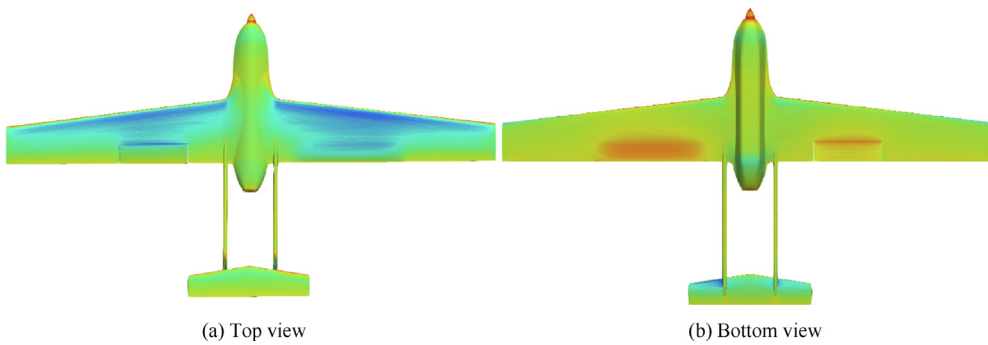

(a) Top view

(b) Bottom view

Fig. 13 Pressure contours of a UAS-S45 with a hinged flap and an SMTE flap.

(a) UAS-S45

(b) Hinged flap   (c) SMTE flap
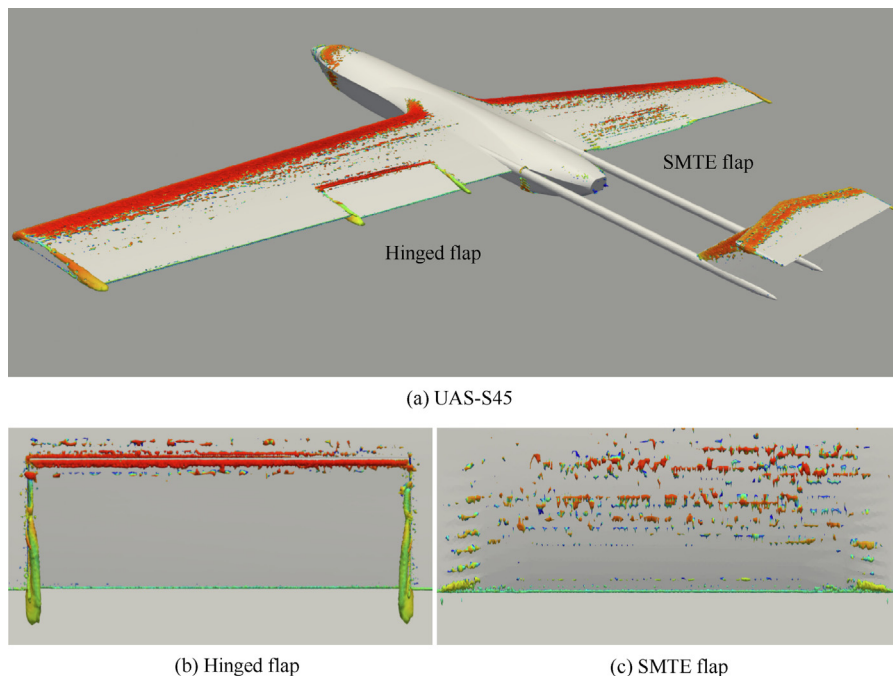
Fig. 14   Vorticity contour comparison of UAS-S45, with hinged flap, and SMTE flap.

(a) Lift coefficient

(b) Drag coefficient

(c) Endurance efficiency
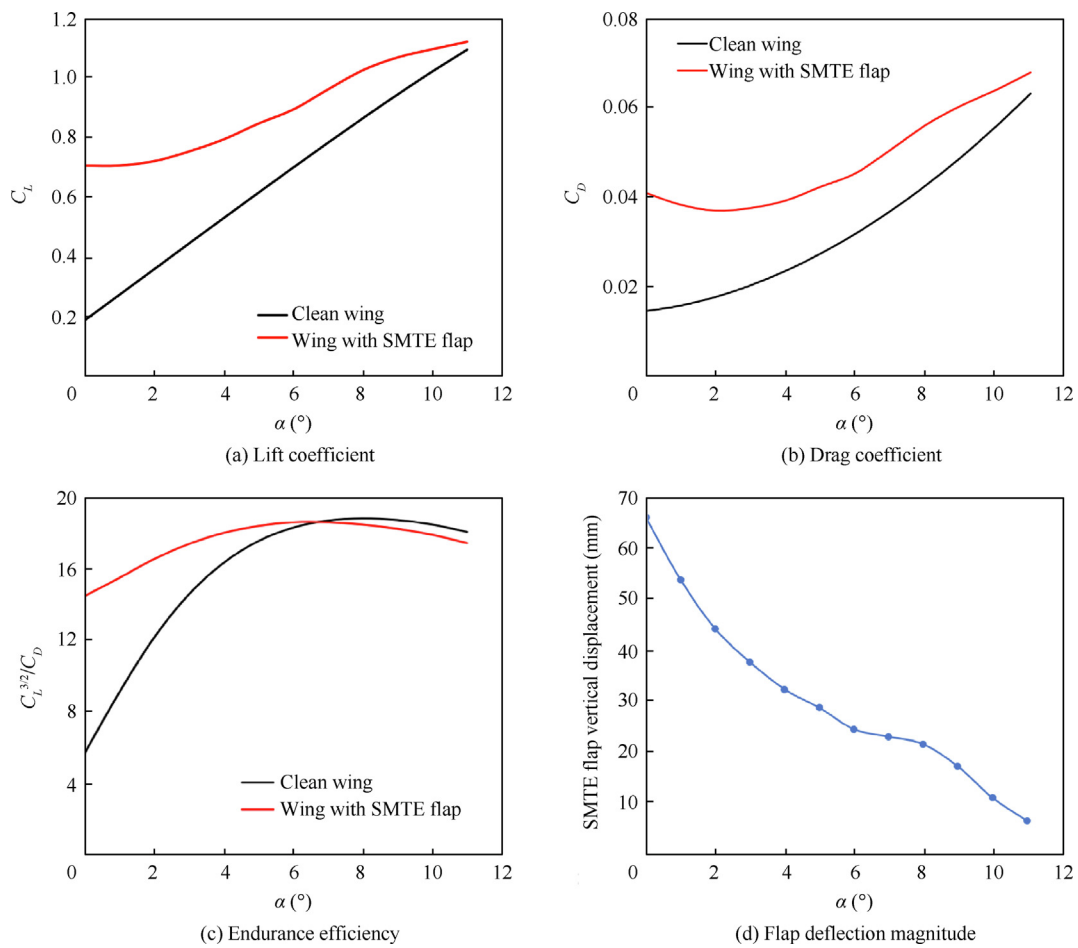

(d) Flap deflection magnitude

Fig. 15   Performance of wing with an SMTE flap vs clean wing for different angles of attack.
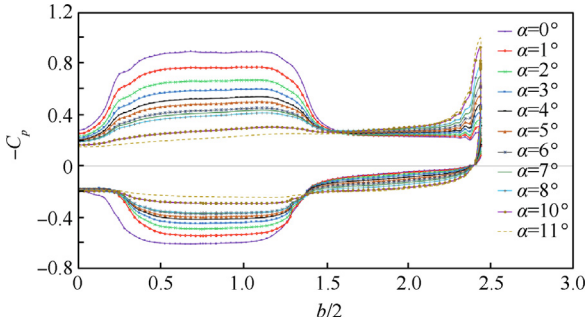
Fig. 16 Spanwise pressure coefficient for UAS-S45 wing with SMTE flap.

power involved in the whole distance from the orbit to the landing lane; a good equilibrium of the lift, drag and weight is used for landing the shuttle without any need for propulsive forces. Sailplanes are another example of gliding descent. Nonetheless, non-powered descent is not a normal flight condition for most aircraft, and it most often only occurs because of engine failure which calls for emergency measures. In this critical situation, the pilot's highest priority is to have more time to prepare for an emergency landing or to restart the engine; therefore, reducing the descent rate is the only option for extending the descent time.

In gliding descent, only the aerodynamic forces will guarantee the safety of the aircraft; therefore, establishing a suitable equilibrium among these forces is decisive. The only forces acting on the aircraft in the gliding descent are the lift, drag and weight, where the latter is almost non-variable (if overlooking the fuel weight), and only the lift and drag forces remain as crucial aerodynamic forces. This means that by choosing the optimum angle of attack and angle of deflection for the aircraft, the descent time can be extended, or in other words, the descent rate can be decreased as much as possible. In the same way as for the climb condition, in gliding descent, the small angle assumption is considered (angles between $-5°$ and $-15°$); however, since this is a descent condition, only the negative values in this range are considered. Fig. 17 shows the UAS-S45 in gliding descent condition with the aerodynamic forces acting on it.

The equilibrium of aerodynamic forces along the trajectory reflects the relationship between drag and weight (Eq. (21)),

and in the perpendicular direction, given the small angle assumption ($\cos \gamma \approx 1$), we have $L = W$.

$$-D + W\sin\gamma = 0 \tag{21}$$

By replacing W with L and multiplying all terms by velocity, the following equation is obtained.

$$V\sin\gamma = \frac{DV}{L}$$
or
$$\frac{\mathrm{d}h}{\mathrm{d}t} = V\frac{C_D}{C_L} \tag{22}$$

Using the small angle assumption, the velocity becomes:

$$V = \sqrt{\frac{2W}{\rho S C_L}} \tag{23}$$

Finally, by replacing Eq. (23) in Eq. (22), the ultimate equation for the descent rate becomes:

$$\frac{\mathrm{d}h}{\mathrm{d}t} = \sqrt{\frac{2W}{\rho S}} \cdot \frac{C_D}{C_L^{3/2}} \tag{24}$$

Eq. (24) indicates that by minimizing the aerodynamic term $C_D/C_L^{3/2}$, which is the objective function, the descent rate is decreased; therefore, the objective function is defined as the minimization of $C_D/C_L^{3/2}$.

The values of $C_D/C_L^{3/2}$ are studied for a number of four different angles of descent, from $-5°$ to $-8°$ (all are within the small angle assumption range) to find the best angle of descent as well as the best angle of deflection for the SMTE flap versus the clean wing. Fig. 18 shows the optimization results of the UAS-S45 wing with an SMTE flap, where the objective function ($C_D/C_L^{3/2}$) is minimized for different angles of attack.

As illustrated in Fig. 18, for all angles of attack the morphing flap deformation has minimized the descent rate compared to a wing with no flap. Evaluating the reduction of the rates of descent, the maximum reduction belongs to $\gamma = -5°$, with its 43% reduction in the descent rate, which is nearly half the normal descent rate. However, the minimum descent rate belongs to $\gamma = -6°$, where $C_D/\left|C_L^{3/2}\right| = 0.1$, meaning that, although the maximum minimization occurs at $\gamma = -5°$ (43%), it is not the minimum descent rate among the studied angles of attack ($C_D/\left|C_L^{3/2}\right| = 1.1$). Therefore, $\gamma = -6°$ is chosen as the optimum angle of descent, at which the minimum descent

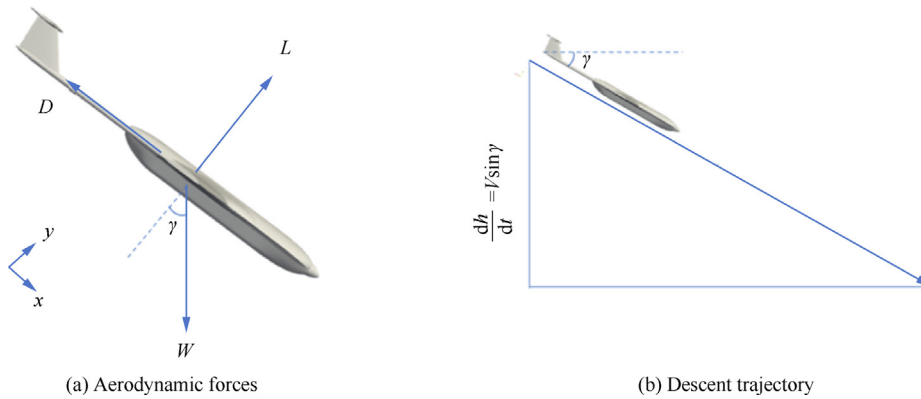
(a) Aerodynamic forces

(b) Descent trajectory

Fig. 17 UAS-S45 in descent flight conditions with its aerodynamic forces and descent trajectory.
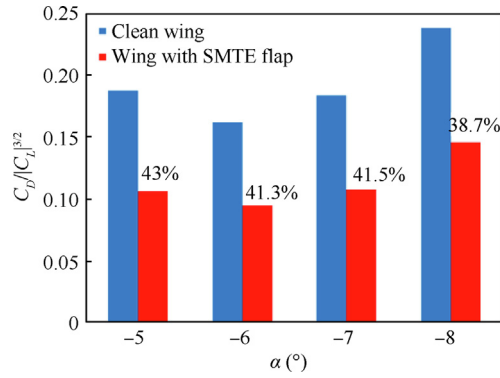
Fig. 18 Comparison of descent rate between a clean wing and a wing with an SMTE flap.
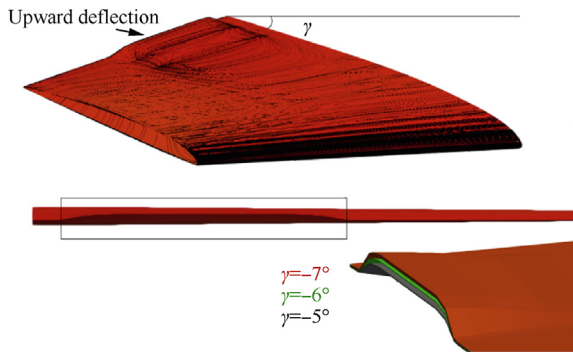

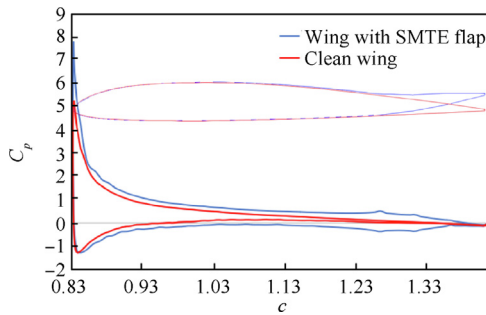**Fig. 19** Optimum configuration of a UAS-S45 wing equipped with an SMTE flap for gliding descent flight.

Fig. 20 Pressure coefficient variations around a wing with an SMTE flap and around a clean wing at $\gamma == -7°$.

rate occurs. It can be deduced that by an optimum deformation of the SMTE flap in the gliding descent condition, an efficient equilibrium of aerodynamic forces is produced to reduce the descent rate as much as possible. Note that since the lift coefficient in descent is negative, the absolute value of the lift is used in Fig. 18. Unlike the previous flight conditions, e.g., climb and cruise, where the optimum deformation of the SMTE flap was in the downwards direction, in descending flight, due to the negative angle of descent, the optimal deformation of the flap is oriented in the upwards direction, and as the descent angle increases, the deformation also increases in

the upwards direction (Fig. 19). Note that for better illustration, the absolute value of lift coefficient is represented, since in descent flight the generated lift is always negative.

In addition, Fig. 20 shows the pressure coefficient variations around a wing with an SMTE flap and for a clean wing at $\gamma = -7°$. The pressure coefficient variations indicate a pressure gap, through which the magnitude of negative lift force increases and since the variation of drag due to flap deflection is not high, the ultimate objective function, which is $C_D/C_L^{3/2}$, is decreased, thus accomplishing the goal of reducing the gliding descent rate.

4. Conclusions

This study investigated the seamless morphing trailing edge flap (SMTE flap) for the whole flight envelope of a UAS-S45, including climb, cruise, and gliding descent, each of which have their unique specific flight characteristics. The main objective of this study was to find the optimum configuration of the SMTE flap for these three flight conditions with their corresponding objective functions and goals.

For the climb condition, the goal was to find an optimum configuration to increase the climb rate compared to that of the clean wing configuration, and this goal was accomplished by decreasing the required engine power to its minimum rate. The results showed that by decreasing the required power to a minimum rate by up to 3.8%, the climb rate could increase by 6.13%.

The cruise flight condition had two objectives, range, and endurance improvement, depending on the flight mission objective. The goal was to increase both the range and endurance, and to find the optimum SMTE flap configuration for each of them. Regarding the range improvement, the SMTE flap was compared with the hinged flap configuration in terms of aerodynamic performance, and it was shown the SMTE flap out-performed the hinged flap in many aspects. These aspects included extending laminar flow on wing upper surface, improving the flow stability by restricting its turbulence behavior, and improving the aerodynamic performance by generating excessive lift by sealing the gaps in the transition sections, increasing the lift-to-drag ratio by up to 17.8% compared to the hinged flap, and by up to 33% compared to the clean wing configuration. Finally, the optimum angle of attack was determined for achieving maximum range. In the next step, the optimum configuration and angle of attack were found for maximizing the endurance; therefore, a 61.2% gain was achieved for endurance of the SMTE flap compared to that of the clean wing configuration.

In the final section, the gliding descent phase was studied with the purpose of reducing the descent rate by using an SMTE flap. Unlike the other flight conditions, where the optimum configuration of the flap was oriented in the downwards direction during the gliding descent, the optimum SMTE flap was deflected upwards, which minimized the descending rate for a number of four negative angles of descent. The maximum reduction of descent rate compared to baseline wing was up to 43% for $\gamma = -5°$, however, the minimum magnitude of the descent rate was achieved for $\gamma = -6°$, which was chosen as the optimum angle of attack for gliding descent.

This study showed the advantages of using SMTE flaps instead of conventional hinged flaps and found the optimum

SMTE flap configuration for three flight phases of an UAS-S45, by which the aircraft could achieve its highest flight performance. In this study, only three main flight conditions are considered, while other phases such as cruise climb, loiter, and cruise descent will be presented in further studies. In addition, this study has considered only the aerodynamic aspects of the SMTE flap and other aspects such as actuation mechanism, structural weight and actuation control will be analyzed and presented in the future paper. For morphing aircraft, aerodynamics, structure, and control disciplines are coupled; therefore, in our next study, the structural and control aspects of an SMTE flap will be investigated by proposing a novel trailing edge actuation mechanism to analyze its structural feasibility and sustainability by utilizing the target optimized shapes of the SMTE flap obtained from this study. In addition, structural optimization will be performed in terms of structural weight minimization.

Declaration of competing interest

The authors declare that they have no known competing financial interests or personal relationships that could have appeared to influence the work reported in this paper.

Acknowledgements

References

1. Jacobo J. How coronavirus impacts climate change with emissions reductions[Internet]. [cited 2023 Jan 12]. Available from: https://abcnews.go.com/International/severe-reduction-emissions-corona-virus-mitigate-climate-change-long/story?id = 69334246.
2. Le Quéré C, Jackson RB, Jones MW, et al. Temporary reduction in daily global CO_2 emissions during the COVID-19 forced confinement. *Nat Clim Chang* 2020;**10**(7):647–53.
3. fello'fly[internet]. Leiden: Airbus; [cited 2023 Jan 12]. Available from: https://www.airbus.com/en/innovation/disruptive-concepts/biomimicry/fellofly.
4. Concilio A, Dimino I, Pecora R, et al. *Morphing wing technologies: Large commercial aircraft and civil helicopters*. Cambridge: Cambridge University Press; 2017.
5. Ameduri S, Concilio A. Morphing wings review: Aims, challenges, and current open issues of a technology. *Proc Inst Mech Eng C J Mech Eng Sci* 2020;**237**(18):095440622094442.
6. Muhammad Umer H, Maqsood A, Riaz R, et al. Stability characteristics of wing span and sweep morphing for small unmanned air vehicle: A mathematical analysis. *Math Probl Eng* 2020;**2020**:1–15.
7. Segui M, Botez RM, Paper É, et al. Evaluation of the impact of morphing horizontal tail design of the UAS-S45 performances. Environmental Science [Internet]. 2019 [cited 2023 Jan 12]; Available from: https://api.semanticscholar.org/CorpusID:250406458.
8. Ismail NI, Zulkifli AH, Abdullah MZ, et al. Optimization of aerodynamic efficiency for twist morphing MAV wing. *Chin J Aeronaut* 2014;**27**(3):475–87.
9. Segui M, Abel FR, Botez RM, et al. New aerodynamic studies of an adaptive winglet application on the regional jet CRJ700. *Biomimetics* 2021;**6**(4):54.
10. Liauzun C, Le Bihan D, David J-M, et al. Study of morphing winglet concepts aimed at improving load control and the aeroelastic behavior of civil transport aircraft. *Aerospace Lab* 2018;**14**:1–15.
11. Ajaj R, Friswell M, Saavedra Flores E, et al. Span morphing: A conceptual design study. *Proceedings of the 53rd AIAA/ASME/ASCE/AHS/ASC structures, structural dynamics and materials conference; 20th AIAA/ASME/AHS adaptive structures conference; 14th AIAA*. Honolulu, Hawaii. Reston: AIAA; 2012.
12. Communier D, Botez RM, Wong T. Design and validation of a new morphing camber system by testing in the price—Païdoussis subsonic wind tunnel. *Aerospace* 2020;**7**(3):23.
13. Negahban MH, Botez RM, Razavi SE. New method for the flow modeling around chord-wise morphing airfoil. *Proceedings of the AIAA scitech 2022 forum*. Reston: AIAA; 2022.
14. Razavi SE, Negahban MH. Numerical investigation of flow behavior around chordwise morphing NACA 0012. *Amirkabir J Mech Eng* 2020;**51**(6):1411–26.
15. Li YZ, Ge WJ, Zhou J, et al. Design and experiment of concentrated flexibility-based variable camber morphing wing. *Chin J Aeronaut* 2022;**35**(5):455–69.
16. Negahban MH, Bashir M, Botez RM. Aerodynamic optimization of a novel synthetic trailing edge and chord elongation morphing: Application to the UAS-S45 airfoil. *Proceedings of the AIAA scitech 2023 forum*. Reston: National Harbor; 2023.
17. Bashir M, Longtin-Martel S, Botez RM, et al. Optimization and design of a flexible droop-nose leading-edge morphing wing based on a novel black widow optimization algorithm—part I. *Designs* 2022;**6**(1):10.
18. Bashir M, Longtin-Martel S, Zonzini N, et al. Optimization and design of a flexible droop nose leading edge morphing wing based on a novel black widow optimization (B.W.O.) algorithm—part II. *Designs* 2022;**6**(6):102.
19. Kan Z, Li DC, Shen T, et al. Aerodynamic characteristics of morphing wing with flexible leading-edge. *Chin J Aeronaut* 2020;**33**(10):2610–9.
20. Koreanschi A, Sugar Gabor O, Acotto J, et al. Optimization and design of an aircraft's morphing wing-tip demonstrator for drag reduction at low speed, Part I-Aerodynamic optimization using genetic, bee colony and gradient descent algorithms. *Chin J Aeronaut* 2017;**30**(1):149–63.
21. Botez RM, Molaret P, Laurendeau E. Laminar flow control on a research wing project presentation covering a three year period. *Canadian aeronautics and space institute annual general meeting*. 2007.
22. Sugar Gabor O. Validation of morphine wing methodologies on an unmanned aerial system and a wind tunnel technology demonstrator. *École de technologie supérieure*. 2015.
23. Gabor OŞ, Simon A, Koreanschi A, et al. Improving the UAS-S4 Éhecal airfoil high angles-of-attack performance characteristics using a morphing wing approach. *Proc Inst Mech Eng Part G* 2016;**230**(1):118–31.
24. Şugar Gabor O, Koreanschi A, Botez RM. Analysis of UAS-S4 Éhecatl aerodynamic performance improvement using several configurations of a morphing wing technology. *Aeronaut J* 2016;**120**(1231):1337–64.
25. Botez RM, Koreanschi A, Gabor OS, et al. Numerical and experimental transition results evaluation for a morphing wing and aileron system. *Aeronaut J* 2018;**122**(1251):747–84.
26. Popov AV, Grigorie LT, Botez R, et al. Real time morphing wing optimization validation using wind-tunnel tests. *J Aircr* 2010;**47**(4):1346–55.
27. Popov AV, Botez RM, Labib M. Transition point detection from the surface pressure distribution for controller design. *J Aircr* 2008;**45**(1):23–8.

28. Koreanschi A, Gabor OS, Acotto J, et al. Optimization and design of an aircraft's morphing wing-tip demonstrator for drag reduction at low speeds, Part II - Experimental validation using infrared transition measurement from wind tunnel tests. *Chin J Aeronaut* 2017;**30**(1):164–74.

29. Şugar Gabor O, Koreanschi A, Botez RM. A new non-linear vortex lattice method: Applications to wing aerodynamic optimizations. *Chin J Aeronaut* 2016;**29**(5):1178–95.

30. Carossa GM, Ricci S, De Gaspari A, et al. Adaptive trailing edge: Specifications, aerodynamics, and exploitation. *Smart intelligent aircraft structures (SARISTU)*. Cham: Springer; 2016. p. 143–58.

31. Pecora R, Magnifico M, Amoroso F, et al. Multi-parametric flutter analysis of a morphing wing trailing edge. *Aeronaut J* 2014;**118**(1207):1063–78.

32. Burdette DA, Kenway GK, Lyu ZJ, et al. Aerostructural design optimization of an adaptive morphing trailing edge wing. *Proceedings of the 56th AIAA/ASCE/AHS/ASC structures, structural dynamics, and materials conference*; Kissimmee, Florida. Reston: AIAA; 2015.

33. Dumont A. Adjoint-based aerodynamic shape optimization applied to morphing technology on a regional aircraft wing. *Morphing wing technologies*. Amsterdam: Elsevier; 2018. p. 145–74.

34. Li B, Li G. Analysis and optimization of a camber morphing wing model. *Int J Adv Rob Syst* 2016;**13**(5):172988141666484.

35. You H, Kim S, Joe WY, et al. New concept for aircraft morphing wing skin: design, modeling, and analysis. *AIAA J* 2019;**57**(5):1786–92.

36. Murugan S, Woods BKS, Friswell MI. Hierarchical modeling and optimization of camber morphing airfoil. *Aerosp Sci Technol* 2015;**42**:31–8.

37. Amendola G, Dimino I, Magnifico M, et al. Distributed actuation concepts for a morphing aileron device. *Aeronaut J* 2016;**120**(1231):1365–85.

38. Pecora R. Morphing wing flaps for large civil aircraft: Evolution of a smart technology across the Clean Sky program. *Chin J Aeronaut* 2021;**34**(7):13–28.

39. Hao FQ, Tang T, Gao YA, et al. Continuous morphing trailing-edge wing concept based on multi-stable nanomaterial. *Chin J Aeronaut* 2021;**34**(7):219–31.

40. Liu WD, Zhu H, Zhou SQ, et al. In-plane corrugated cosine honeycomb for 1D morphing skin and its application on variable camber wing. *Chin J Aeronaut* 2013;**26**(4):935–42.

41. Wu R, Soutis C, Zhong S, et al. A morphing aerofoil with highly controllable aerodynamic performance. *Aeronaut J* 2017;**121**(1235):54–72.

42. Takahashi H, Yokozeki T, Hirano Y. Development of variable camber wing with morphing leading and trailing sections using corrugated structures. *J Intell Mater Syst Struct* 2016;**27**(20):2827–36.

43. Nguyen NT, Livne E, Precup N, et al. Experimental investigation of a flexible wing with a variable camber continuous trailing edge flap design. *Proceedings of the 32nd AIAA applied aerodynamics conference*; Atlanta, GA. Reston: AIAA; 2014.

44. Communier D, Le Besnerais F, Botez RM, et al. Design, manufacturing, and testing of a new concept for a morphing leading edge using a subsonic blow down wind tunnel. *Biomimetics* 2019;**4**(4):76.

45. Arena M, Amoroso F, Pecora R, et al. Numerical and experimental validation of a full scale servo-actuated morphing aileron model. *Smart Mater Struct* 2018;**27**(10):105034.

46. Pecora R, Amoroso F, Magnifico M, et al. KRISTINA: Kinematic rib-based structural system for innovative adaptive trailing edge. SPIE smart structures and materials + nondestructive evaluation and health monitoring. *Proc SPIE 9801, industrial and commercial applications of smart structures technologies 2016*; Las Vegas, Nevada, USA. 2016;**9801**:67–77.

47. Concilio A, Dimino I, Pecora R, et al. Structural design of an adaptive wing trailing edge for enhanced cruise performance. *Proceedings of the 24th AIAA/AHS adaptive structures conference*; San Diego, California, USA. Reston: AIAA; 2016.

48. Powers S, Webb L, Friend E, et al. Flight test results from a supercritical mission adaptive wing with smooth variable camber. *Proceedings of the 6th AIAA biennial flight test conference*; Hilton Head, SC. Reston: AIAA; 1992.

49. Kota S, Flick P, Collier F. Flight testing of the FlexFloil™ adaptive compliant trailing edge. *54th AIAA aerospace sciences meeting*. Reston: AIAA; 2016.

50. Miller EJ, Cruz J, Lung SF, et al. Evaluation of the hinge moment and normal force aerodynamic loads from a seamless adaptive compliant trailing edge flap in flight. *Proceedings of the 54th AIAA aerospace sciences meeting*; San Diego, California, USA. Reston: AIAA; 2016.

51. Kota S, Osborn R, Ervin GF. Mission adaptive compliant wing–design, fabrication and flight test. *RTO applied vehicle technology panel (AVT) symposium*. 2009. p. 1–18.

52. Abdessemed C, Yao YF, Bouferrouk A, et al. Analysis of a 3D unsteady morphing wing with seamless side-edge transition. *Proceedings of the 2018 applied aerodynamics conference*; Atlanta, Georgia. Reston: AIAA; 2018.

53. Chawki A, Yao YF, Abdessalem B, et al. Morphing airfoils analysis using dynamic meshing. *Int J Numer Meth Heat Fluid Flow* 2018;**28**(5):1117–33.

54. Abdessemed C, Bouferrouk A, Yao YF. Effects of an unsteady morphing wing with seamless side-edge transition on aerodynamic performance. *Energies* 2022;**15**(3):1093.

55. Ting E, Chaparro D, Nguyen N, et al. Optimization of variable-camber continuous trailing-edge flap configuration for drag reduction. *J Aircr* 2018;**55**(6):2217–39.

56. Ting E, Chaparro D. Nguyen NT. Aero-structural optimization of variable camber continuous trailing edge flap configurations using transonic and viscous potential flow method. *Proceedings of the 35th AIAA applied aerodynamics conference*; Denver, Colorado. Reston: AIAA; 2017.

57. Urnes J, Nguyen N. A mission adaptive variable camber flap control system to optimize high lift and cruise lift to drag ratios of future n+ 3 transport aircraft. *Proceedings of the 51st AIAA aerospace sciences meeting including the new horizons forum and aerospace exposition*. Reston: AIAA; 2013.

58. Lebofsky S, Ting E, Nguyen NT. Multidisciplinary drag optimization of reduced stiffness flexible wing aircraft with variable camber continuous trailing edge flap. *Proceedings of the 56th AIAA/ASCE/AHS/ASC structures, structural dynamics, and materials conference*; Kissimmee, Florida. Reston: AIAA; 2015.

59. Woods BKS, Parsons L, Coles AB, et al. Morphing elastically lofted transition for active camber control surfaces. *Aerosp Sci Technol* 2016;**55**:439–48.

60. Ninian DA, Dakka S. Design, development and testing of shape shifting wing model. *Aerospace* 2017;**4**(4):52.

61. Pankonien AM, Inman DJ. Aerodynamic performance of a spanwise morphing trailing edge concept. *25th international conference on adaptive structures and technologies*. 2014.

62. Chae EJ, Moosavian A, Pankonien AM, et al. A comparative study of a morphing wing. *Proceedings of ASME 2017 conference on smart materials, adaptive structures and intelligent systems*; Snowbird, Utah, USA. 2017.

63. Rodriguez DL, Aftosmis MJ, Nemec M, et al. Optimized off-design performance of flexible wings with continuous trailing-edge flaps. *Proceedings of the 56th AIAA/ASCE/AHS/ASC structures, structural dynamics, and materials conference*; Kissimmee, Florida. Reston: AIAA; 2015.

64. Lyu ZJ, Martins JRRA. Aerodynamic shape optimization of an adaptive morphing trailing-edge wing. *J Aircr* 2015;**52**(6):1951–70.

65. Communier D, Botez RM, Wong T. Experimental validation of a new morphing trailing edge system using Price - Païdoussis wind tunnel tests. *Chin J Aeronaut* 2019;**32**(6):1353–66.

66. Bashir M, Longtin-Martel S, Botez RM, et al. Aerodynamic design optimization of a morphing leading edge and trailing edge airfoil–application on the UAS-S45. *Appl Sci* 2021;**11**(4):1664.

67. Khorrami MR, Lockard DP, Moore JB, et al, inventors; The United States of America represented by the Administrator of the National Aeronautics and Space Administration. Elastically deformable side-edge link for trailing-edge flap aeroacoustic noise reduction. United States Patent US 8,695,925 B2. 2014 Apr 15.

68. Rivero AE, Fournier S, Manolesos M, et al. Experimental aerodynamic comparison of active camber morphing and trailing-edge flaps. *AIAA J* 2021;**59**(7):2627–40.

69. Kuitche MAJ, Botez RM. Modeling novel methodologies for unmanned aerial systems - Applications to the UAS-S4 Ehecatl and the UAS-S45 Bálaam. *Chin J Aeronaut* 2019;**32**(1):58–77.

70. Wächter A, Biegler LT. On the implementation of an interior-point filter line-search algorithm for large-scale nonlinear programming. *Math Program* 2006;**106**(1):25–57.

71. Ipopt Documentation hc-ogiI[Internet]. Available from: https://github.com/coin-or/Ipot.

72. Towara M, Naumann U. A discrete adjoint model for OpenFOAM. *Procedia Comput Sci* 2013;**18**:429–38.

73. He P, Mader CA, Martins JRRA, et al. DAFoam: an open-source adjoint framework for multidisciplinary design optimization with OpenFOAM. *AIAA J* 2020;**58**(3):1304–19.

74. He P, Mader CA, Martins JRRA, et al. An object-oriented framework for rapid discrete adjoint development using OpenFOAM. *Proceedings of the AIAA scitech 2019 forum*; San Diego, California. Reston: AIAA; 2019.

75. Gebremedhin AH, Manne F, Pothen A. What color is your Jacobian? Graph coloring for computing derivatives. *SIAM Rev* 2005;**47**(4):629–705.

76. Masters DA, Taylor NJ, Rendall T, et al. Review of aerofoil parameterisation methods for aerodynamic shape optimisation. *Proceedings of the 53rd AIAA aerospace sciences meeting*; Kissimmee, Florida. Reston: AIAA; 2015.

77. Sederberg TW, Parry SR. Free-form deformation of solid geometric models. *Proceedings of the 13th annual conference on computer graphics and interactive techniques*. New York: ACM; 1986. p. 151–60.

78. Coquillart S. Extended free-form deformation: A sculpturing tool for 3D geometric modeling. *Proceedings of the 17th annual conference on computer graphics and interactive techniques*. New York: ACM; 1990. p. 187–96.

79. Lamousin HJ, Waggenspack NN. NURBS-based free-form deformations. *IEEE Comput Graph Appl* 1994;**14**(6):59–65.

80. Ronzheimer A. Shape parameterisation based on freeform deformation in aerodynamic design optimization. *ERCOFTAC design optimization. Methods & applications* 2004;400.

81. Samareh J. Aerodynamic shape optimization based on free-form deformation. *Proceedings of the 10th AIAA/ISSMO multidisciplinary analysis and optimization conference*; Albany, New York. Reston: AIAA; 2004.

82. Samareh J. Multidisciplinary aerodynamic-structural shape optimization using deformation (MASSOUD). *Proceedings of the 8th symposium on multidisciplinary analysis and optimization*; Long Beach, CA, USA. Reston: AIAA; 2000.

83. Ronzheimer A. Prospects of geometry parameterization based on freeform deformation in MDO. *ERCOFTAC 2006 international conference*. 2006.

84. Kenway G, Kennedy G, Martins JRRA. A CAD-free approach to high-fidelity aerostructural optimization. *Proceedings of the 13th AIAA/ISSMO multidisciplinary analysis optimization conference*; Fort Worth, Texas. Reston: AIAA; 2010.

85. Negahban MH, Bashir M, Botez RM. Free-form deformation parameterization on the aerodynamic optimization of morphing trailing edge. *Appl Mech* 2023;**4**(1):304–16.

86. Marchman JF. *Aerodynamics and aircraft performance*. Blacksburg(VA): University Libraries at Virginia Tech.; 2004.